Received: 31 December 2024 | Revised: 19 March 2025 | Accepted: 20 March 2025

DOI: 10.1111/jace.20547

Journal of the American Ceramic Society

RESEARCH ARTICLE

Effect of groove-like structures on residual stress and shear strength in C/SiC–C103 alloy joints

Anurag Kamal[1,2] | **Mahendra Kumar Pal**[3] | **Vijay M. Shinde**[1] | **Aniket B. Jadhav**[1] | **Anoop Kumar Shukla**[4]

[1]Department of Chemical Engineering, Indian Institute of Technology (BHU), Varanasi, India

[2]Ceramic Matrix Products Division (CMDG/CMSE), Vikram Sarabhai Space Centre, Indian Space Research Organization (ISRO), Thiruvananthapuram, India

[3]Department of Civil Engineering, Indian Institute of Technology (BHU), Varanasi, India

[4]Special Metallurgical Facilities (MMG/MME), Vikram Sarabhai Space Centre, Indian Space Research Organization (ISRO), Thiruvananthapuram, India

Correspondence
Vijay M. Shinde, Department of Chemical Engineering, Indian Institute of Technology (BHU), Varanasi, 221005, India.
Email: vijay.che@iitbhu.ac.in

Abstract

The study integrates a groove-like structure (GLS) into C/SiC composites utilizing Ticusil® braze alloy, leading to decreased residual stress and fortified joint connections with the C103 alloy. The primary joining mechanisms involve the infiltration of molten alloy into the composite, leading to the formation of a continuous thin $TiCu_2$ layer near the brazing seam and a TiC/Ti_5Si_3 layer at the metal–ceramic interface. The residual stresses in the joints and their concentration sites are determined using the finite element method. The effects of GLS configurations including width, depth, and spacing on microstructure, composition, and residual stress, as well as potential crack sites, are comprehensively evaluated and compared to experimental results. GLS behavior under loading conditions is also inferred, in part, by predicting stress paths via shear strength simulations. An optimal GLS configuration with 1 mm depth, width, and spacing is identified that yields a shear strength of 22.8 MPa, 99% of that of a C/SiC composite strength.

KEYWORDS
brazing, C/SiC, joining, microstructure, structural applications

1 | INTRODUCTION

Fiber-reinforced silicon carbide matrix composites (C/SiC), consisting of a carbon fiber network embedded within a silicon carbide matrix, offer superior thermophysical and thermomechanical properties compared to metallic materials.[1] These properties include low density, high thermal conductivity, exceptional strength and toughness, as well as excellent resistance to oxidation and corrosion. As a result, C/SiC composites find widespread applications in the aerospace, nuclear, automotive, defense, and optical industries.[2–5] However, fabricating large or complex C/SiC components can be expensive and challenging. Many structural applications require integrating C/SiC composites with metallic parts. A notable example is the assembly of an extendable thrust chamber for a rocket engine, where the C103 niobium alloy structure is often connected to C/SiC through a Ti-alloy-based fuel injector system.[6]

Despite the aforementioned advantages, joining C/SiC to metals presents significant challenges. These include the nonwettability of C/SiC, susceptibility to process-induced microcracks, formation of brittle intermetallic compounds (IMCs), and high residual stresses caused by the mismatch in the coefficient of thermal expansion (CTE) between C/SiC and metals. Therefore, developing reliable joining technologies between C/SiC composites and C103 niobium alloy is crucial for expanding their use in advanced engineering applications.

Various techniques have been explored for joining C/SiC composites to metals, including brazing,[7] diffusion bonding,[8] transient liquid phase diffusion bonding (TLP-DB),[9] and spark plasma sintering.[10] Diffusion bonding and spark plasma sintering are unsuitable for large-scale component manufacturing due to their extremely high processing temperatures (>1500°C) and significant pressure requirements (>30 MPa). Additionally, TLP-DB is further limited by its prolonged holding times and the necessity for multiple processing steps. In contrast, brazing emerges as a more favorable alternative due to its simplicity, lower processing temperatures, and high repeatability.[11,12] This technique has been proven effective in joining C/SiC composites with various titanium alloys, including TiCu–Cu,[9] TiCuAg,[13] TiNi,[14] TiCuNiZr,[15] and TiCoNb.[16] The presence of titanium in the filler alloy promotes a strong chemical interaction with the C/SiC matrix, improving wetting and forming a metallurgically bonded joint. However, significant differences in physical properties, particularly CTE and elastic modulus, between the joining materials can induce residual stresses within the joint, potentially leading to failure during the brazing process. If these residual stresses exceed a critical threshold, failure can occur even during the brazing process. Therefore, minimizing residual stresses is crucial for achieving strong and reliable joints.

Numerous strategies have been implemented to enhance the joint properties of C/SiC composites with metal components by reducing residual stress. These methods include microstructural adjustments to the brazing seam and modifying the substrate surface.[11,13,17–22] One common approach to modifying the microstructure involves incorporating low-CTE particles, fibers, or soft interlayers into the brazing alloy. While this approach has shown significant improvements in the shear strength of brazed joints, the effectiveness of these strategies varies widely across studies. Furthermore, adding particles, fibers, or interlayers can trigger additional chemical reactions, increasing the microstructural complexity of the joint. This makes achieving a uniform joint microstructure and ensuring the even distribution of these reinforcing phases challenging.

In contrast, modifying the substrate surface provides better control over interfacial properties and applies to a wider range of brazing alloys, resulting in improved joint performance. Several methods have been employed to achieve this, including creating wave-like interfaces,[23] drilling microholes,[22] applying preoxidative corrosion,[24] surface texturing through chemical etching,[13] and ceramic texturing.[25] These techniques promote anchoring, pinning, or nailing effects, which help prevent stress concentration at specific locations and increase energy dissipation during mechanical testing, leading to better ceramic–metal joint performance. However, methods like microdrilling require precise control over hole distribution and size, while chemical etching, preoxidation, and texturing may face limitations related to material compatibility and process control. A wave-like interface, on the other hand, generates alternating stress fields that help prevent crack propagation, offering an advantage by eliminating the need for an interlayer, making it well suited for high-temperature applications.

A comprehensive review of the literature highlights wave-like interface structures as one of the most effective, economical, and reproducible methods for managing stress in ceramic–metal joints. Xiong et al. demonstrated the successful use of a rectangular wave interface (RWI) for bonding 2D C/C composites to Ti64, showing that the RWI significantly improved joint strength by reducing stress concentrations under tensile loading.[23] Despite these advancements, critical details on optimizing the geometry of such interfaces—including groove depth, width, and spacing—remain largely unexplored. This gap underscores the need for further investigation into interfacial designs, particularly in C/SiC systems using reactive braze alloys. In this study, we address this need by brazing chemical vapor infiltration (CVI)-derived C/SiC composites to C103 alloy using Ticusil®, a highly reactive braze alloy. The strength of the joint is enhanced by introducing a groove-like structure (GLS) on the C/SiC interface through a straightforward, cost-effective mechanical cutting process. Key geometrical parameters—including groove depth, width, and spacing—are systematically analyzed to assess their effect on the microstructure and mechanical performance of the joints. Finite element analysis (FEA) is employed to map residual stress distribution across different groove configurations, providing valuable insights into reinforcement and fracture mechanisms. Based on these investigations, the optimal interface geometry for enhanced mechanical strength is proposed.

2 | EXPERIMENTAL

2.1 | Materials

A 2.5D eight harness satin-woven carbon fabric (M/s. Toray, Grade: T300) preform was prepared in-house using a through-the-thickness stitching process. A pyrolytic carbon (PyC) interphase coating, ~1 μm thick, was applied using a CVI process with methane as the precursor gas. Subsequently, the preform was deposited with SiC via the CVI process using a mixture containing 10 vol.% methyltrichlorosilane-hydrogen mixture. The resulting

C/SiC composite exhibited a carbon fiber content of approximately 39 vol.%, a density of about 1.9 g/cc, a porosity of around 10 vol.%, a flexural strength of approximately 350 MPa, and an interlaminar shear strength of about 23 MPa. Optical images of the C/SiC composite, presented in Figure S1A, illustrate a dense microstructure with distinct longitudinal and transverse fiber bundles. A closer view (Figure S1B) shows individual fibers within the bundle surrounded by the matrix, also highlighting the presence of voids, which are intrinsic to C/SiC composites. For the brazing studies, Ticusil® brazing filler (300 μm thickness) and C103 alloy were sourced from commercial suppliers: M/s. Maxon Engineering Pvt. Ltd. and M/s. Kalapurna Steel and Engineering Pvt. Ltd., respectively.

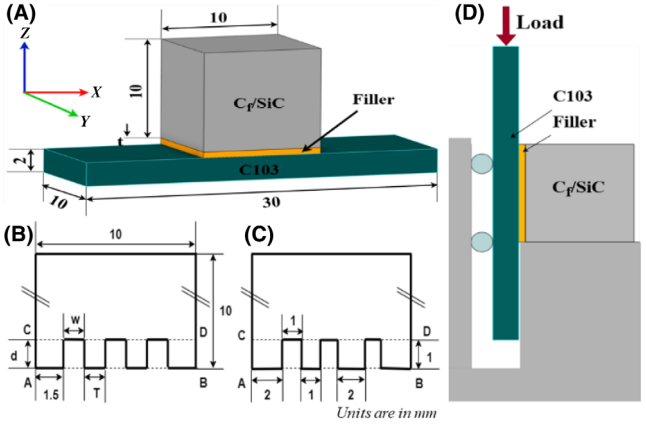

FIGURE 1 Schematic showing (A) brazing configuration, (B, C) specifications of groove-like structure (GLS) created on C/SiC, and (D) lap shear strength (LSS) testing set-up.

2.2 | C/SiC surface modification

The substrates, C/SiC and C103, were machined to dimensions of 30 mm × 10 mm × 2 mm and 10 mm × 10 mm × 5 mm, respectively. In the C/SiC–Ticusil®-C103 brazed joint, the primary concern is the bonding at the C/SiC–Ticusil interface due to the inherent defects in ceramic materials, their nonhomogeneous nature, and the significant CTE mismatch between the ceramic and metal.[6] To improve this, the surface of the C/SiC was modified by introducing a rectangular GLS along the thickness direction using a polycrystalline diamond-coated wheel. This cutting process removes the exterior protective SiC layer, exposing the carbon fibers. To prevent direct interaction between the exposed fibers and the reactive braze, a seal coating of SiC was reapplied using the CVI process. Further, the GLS increases the contact surface area between the brazing alloy and the C/SiC composite, which is critical for enhancing the bonding. The extent of this increased surface area depends on the specific GLS configuration. The change in surface area for different joint types due to GLS can be quantified by the groove structure index (GSI), defined by Equation (1). A higher GSI indicates a larger surface area available for metal–ceramic contact during the brazing process.

$$\text{GSI} = \frac{\text{Surface area at joining interface of GLS}}{\text{Surface area at joining interface of flat}} \quad (1)$$

The dimensions of the GLS within the C/SiC are expected to significantly affect the overall joint performance, making it crucial to optimize the GLS specifications for achieving the best quality joint. In this study, the critical parameters considered were the width (w), depth (d), and the spacing between consecutive grooves (s). As noted by Xiong et al., variations in the groove depth-to-composite thickness ratio (d/H) from 0.05 to 0.3 did not significantly impact the stress distribution. However, excessively high d/H ratios could compromise the structural integrity of the composite.[23] Therefore, this study limited the maximum d/H ratio to 0.2 to preserve the integrity of the joint. Six different joint configurations were analyzed: J-W1D1S1, J-W1D1S2, J-W1D2S1, J-W1D2S2, J-mixed, and J-flat (without GLS). In this nomenclature, W, D, and S represent the width, depth, and spacing between consecutive grooves, respectively. The details of these joint configurations and their corresponding GSIs are presented in Figure 1 and Table 1.

2.3 | Brazing experiment

The joining process for each configuration with the C103 alloy was conducted in a vacuum brazing furnace. Before brazing, the C/SiC substrates, C103 alloy, and Ticusil® braze filler were prepared by polishing with 320-grit abrasive paper. After polishing, the components were ultrasonicated in an isopropyl alcohol (IPA) bath for 30 min to ensure cleanliness and then were dried in an oven to remove any residual IPA or moisture. Once the specimens were prepped, they were arranged on the furnace loading platform as shown in Figure 1A, with a small dead load of 0.25 kg/cm^2 applied to ensure proper contact between the filler and the substrates. The furnace was evacuated to a vacuum pressure below 10^{-3} mbar before beginning the brazing experiment. The brazing was then conducted at 840°C (±5) for 35 min, with both heating and cooling rates controlled at 1°C/min to ensure uniform thermal conditions.

TABLE 1 Details of the various joint configurations and parameters for the Ogden model with and without thermal stresses.

Joint configuration	Filler thickness (μm)	w (mm)	d (mm)	s (mm)	Groove structure index (GSI)	Ogden parameters			
						With residual stress		Without residual stress	
						μ_1	α_1	μ_1	α_1
J-flat	130	0	0	0	1	0.455	3.554	0.423	4.38
J-W1D1S1	165	1	1	1	1.8	1.089	3.457	0.6	4
J-W1D1S2	110	1	1	2	1.6	1.384	2.991	0.79	3.45
J-W1D2S1	120	1	2	1	2.3	4.828	2.271	2.503	2.606
J-W1D2S2	125	1	2	2	1.8	0.5	4.345	0.42	5
J-mixed	155	1	1	1,2	1.6	0.482	3.272	0.413	4

2.4 | LSS test and microstructural characterization

The joint strength was evaluated using lap shear strength (LSS) testing under compression mode, conducted on a universal testing machine (Make: M/s. Instron). The GLS was aligned along the y-direction (see Figure 1A), ensuring that the applied shear load would be transversely deflected, as depicted in Figure 1D. Testing continued until the sample fractured, with a crosshead speed set at 0.5 mm/min. For microstructural analysis of the joint interface cross-sections, both an optical microscope (Make: Olympus) and an scanning electron microscopy (SEM; Make: Zeiss) with an accelerating voltage of 15 kV were employed. Elemental analysis at the joint interface was performed using energy-dispersive X-ray spectroscopy (EDS; Make: M/s. Bruker). The X-ray diffraction (XRD) patterns were recorded using a Philips instrument at a temperature of 25°C, with a step size of 0.02° and a step time of 0.5 s, employing Cu-Kα radiation ($\lambda = 1.5418$ Å). Further analysis of the fracture characteristics was carried out using SEM-EDS on the LSS-tested surface, providing detailed insights into the failure mode.

2.5 | Simulation of residual stresses and LSS test

Finite element modeling was conducted on various joint configurations to evaluate their performance under lap-shear testing conditions. The modeling process began by simulating the residual stresses induced during the joining process, followed by simulating the LSS test. The C/SiC composite was treated as an orthotropic material, while the C103 alloy and filler were modeled as elastic materials. During the joining process, the filler material underwent phase transitions, heating up to 840°C and then cooling to 20°C. Therefore, temperature-dependent mechanical and physical properties, as outlined in Table S1, were incorporated into the simulation. To reduce computational expense, only half of each geometry was modeled. Meshes were generated using 3D linear hexahedron elements with a minimum size of 0.25 mm. Thermal boundary conditions were applied to the entire geometry, and weak spring constraints were employed to control rigid body motion without significantly affecting the structural response.

To accurately capture the actual joint failure behavior, the LSS modeling was performed under two scenarios: one that incorporated thermal residual stresses and another that excluded them, allowing for an assessment of the effect of these residual stresses on LSS behavior. The LSS test geometry in the first scenario is obtained from a thermal analysis of the brazing process, resulting in deformation and significant residual stress due to differences in CTE. In the second scenario, residual stresses were disregarded, and the LSS test was conducted on an undeformed geometry. In both cases, movement of the specimen in a lateral direction was constrained, while shear loads were applied at the opposite end. Specifically, the composite side and top surfaces were fixed, and a displacement boundary condition was applied to the side face of the C103 superalloy, as illustrated in Figure 1D. The nonlinear stress–strain behavior of the filler material was modeled using the Ogden hyperelastic material model, described by Equations (2) and (3). The material parameters for this Ogden model were determined through a trial-and-error process, as no experimental data were available (see Table 1). Normal and shear stresses were then extracted and are presented in the following sections for all scenarios considered.

$$w = \sum_{i=1}^{n} \frac{\mu_i}{\alpha_i} \left(\lambda_1^{\alpha_i} + \lambda_2^{\alpha_i} + \lambda_3^{\alpha_i} - 3\right) + \sum_{i=1}^{n} \frac{1}{d_i} (J - 1)^{2i} \tag{2}$$

$$\mu_0 = \sum_{i=1}^{n} \frac{\mu_i \alpha_i}{2} \text{ and } K_0 = \frac{2}{d_i} \tag{3}$$

Here, w is the strain energy function, μ_0 is the initial shear modulus, λ is the strain, α is the dimensionless

nonlinearity constant, and K_0 is the initial bulk modulus. Parameters d_1 and n denote the compressibility and material behavior, respectively. Different values of the parameter n represent the different materials such as $n = 1$ denotes neo-Hookean solids and $n = 2$ represents Mooney–Rivlin solids.

The Ogden model parameters, derived from fitting experimental LSS data, closely align with the one-term Ogden model, indicating a similarity in response between the brazing material and materials like natural rubber and soft tissues.[26] Table 1 presents the material parameters obtained through curve fitting. The varied values of parameters μ and α suggest potential phase changes within the brazing material during the brazing process, a hypothesis further supported by microstructural analysis in Section 3.1. While flat joints, J-W1D2S2, and J-mixed exhibit μ values below 1.0, configurations J-W1D1S1, J-W1D1S2, and J-W1D2S1 display μ values exceeding 1.0, with J-W1D2S1 reaching the highest value of 4.828. This suggests that the J-W1D2S1 configuration possesses the greatest shear stiffness, while the flat joint exhibits the lowest. Additionally, the α value is highest for J-W1D2S2 (5.345) and lowest for J-W1D2S1 (2.871), indicating a higher degree of nonlinearity in the material behavior of J-W1D2S2 compared to J-W1D2S1. Further validation through LSS experimental results is necessary to confirm this observation.

Consistent trends are evident in the simulation results when residual stresses are excluded. Specifically, the nonlinearity parameter, α, generally exhibits higher values across most configurations, except for J-W1D2S1 and J-W1D2S2. This suggests that excluding residual stresses leads to an underestimation of the degree of nonlinearity. The reduced α values observed for J-W1D2S1 can likely be attributed to the inability of the simulation to capture local buckling phenomena, which would otherwise contribute to increased nonlinearity. Furthermore, the initial shear modulus parameter, μ, shows lower values in the absence of residual stresses, aligning with the expectation that a material without residual stresses exhibits reduced stiffness, thereby diminishing μ. Overall, neglecting residual stresses in the simulation results in an underestimation of both the shear modulus and the degree of nonlinearity in the stress–strain behavior.

3 | RESULTS AND DISCUSSION

3.1 | Microstructural analysis of the joints

The optical image, SEM micrograph, and EDS elemental mapping for the J-flat configuration are illustrated in Figure 2. In the optical image (Figure 2A), it is evident that the C/SiC and C103 are well bonded, showing an interphase thickness of approximately 130 μm. Notably, there are no visible macrovoids, cracks, or defects at the metal–ceramic junction. The original interphase thickness of 300 μm decreases to about 130 μm during the brazing process due to the diffusion of constituent elements into the substrates, chemical reactions, and material loss at the exposed edges. The SEM image in Figure 2B further validates the strong bonding between the C103 alloy and the braze interphase. However, a higher magnification (as shown in the inset of Figure 2B) reveals a microcrack at the edge of the filler–C/SiC interface.

The morphology of the interphase consists of two distinct zones: gray and white. EDS mapping, shown in Figure 2C, provides detailed insight into the elemental distribution within the joint cross-section. This mapping confirms the qualitative presence of key elements such as Nb, Hf, Ti, Cu, Ag, Si, and C. EDS point analysis was conducted at locations marked by yellow circles in Figure 2B to identify the compounds formed during the reactive brazing process. The elemental composition and potential phases at the joint interface are summarized in Table 2. The atomic percentages at points P1 and P7 correspond to the C103 and C/SiC substrates, respectively. The C103–filler interface at P2 primarily consists of Ag, with minor quantities of Ti, Cu, and Nb, indicating the formation of $TiCu_2$ (Reactions R1 and R2) dispersed within the Ag matrix. Points P3 and P4, located in the gray regions, display similar Ti and Cu content with traces of Ag, suggesting that Ti reacts with Cu to form TiCu and $TiCu_2$ phases while dissolving Ag up to 1.24 at.%. The white region at P5 is identified as a Cu-rich phase, a solid solution (ss) of Cu and Ag, which contains no detectable Ti, indicating the complete depletion of Ti from the central region of the braze toward both substrates during brazing. This phase separation of Cu and Ag aligns with the Cu-Ag phase diagram, where reduced solubility during cooling leads to the precipitation of separate phases below the eutectic point.[27] At point P6, located within the interfacial reaction layer (IRL), Ti, Si, and C are detected, along with traces of Ag. The rapid diffusion of Ti from the filler into the composite results in its reaction with SiC, producing Ti_5Si_3 (Reaction R3) and TiC (Reaction R4), forming a narrow IRL of less than 1 μm thickness at the filler–C/SiC interface. The depletion of Ti toward both substrates creates a Ti-free central region and a reaction zone ~42 μm thick on each side, as illustrated by the Ti mapping in Figure 2C. On the C103 side, Ti reacts with Cu to form TiCu and $TiCu_2$, while at the SiC interface, TiC, Ti_5Si_3, and C are generated. XRD analysis of the C103–C/SiC interphase, as shown in Figure S2, corroborates the phase formation suggested by the EDS point analysis (Table 2). The presence of Cu and Ag is attributed to the original Ticusil filler. The formation of TiC, Ti_5Si_3, TiCu, and $TiCu_2$ phases aligns with

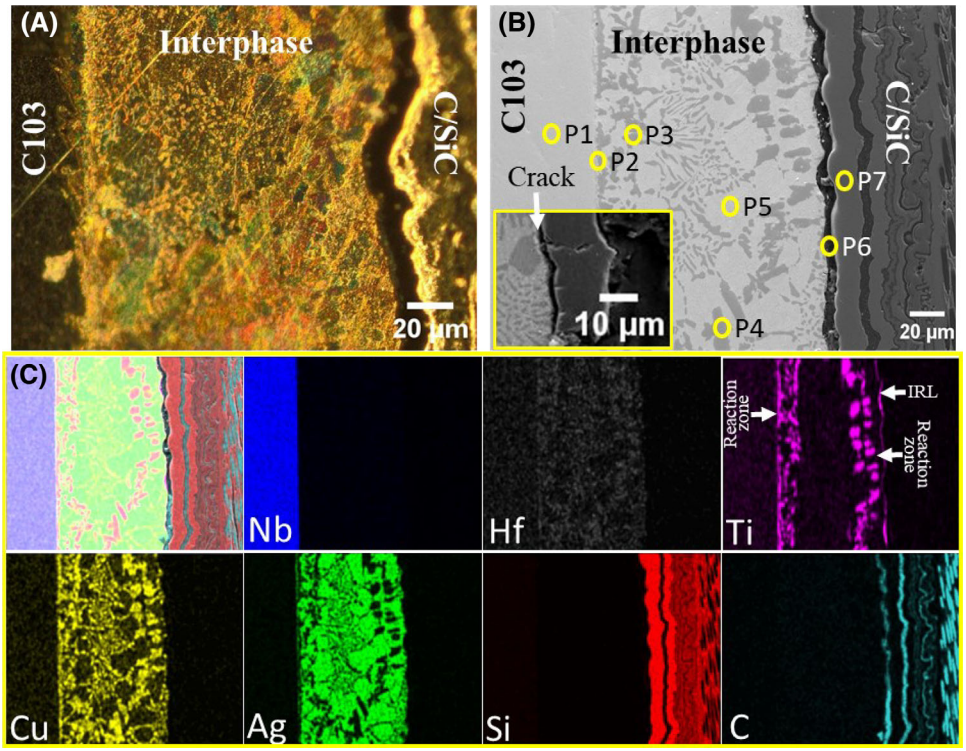

FIGURE 2 (A) Optical image, (B) scanning electron microscopy (SEM) image, (C) energy-dispersive X-ray spectroscopy (EDS) mapping of J-flat.

TABLE 2 Elemental composition and possible phases for the J-flat.

Location	Composition (at.%)							
J-flat	Nb	Hf	Ti	Cu	Ag	Si	C	Possible phases
P1	93.89	3.74	2.36	-	-	-	-	C103
P2	2.13	-	5.44	15.13	77.30	-	-	$TiCu_2$, Ag (s,s)
P3	-	-	45.02	53.94	1.04	-	-	TiCu, $TiCu_2$
P4	-	-	41.60	57.16	1.24	-	-	TiCu, $TiCu_2$
P5	-	-	-	71.57	28.43	-	-	Cu (s,s), Ag (s,s)
P6	-	-	27.79	-	1.00	19.06	52.15	TiC, Ti_5Si_3
P7	-	-	-	-	-	52.73	47.27	SiC

the EDS findings. Furthermore, the presence of free carbon peaks in the XRD results indicates incomplete consumption of carbon atoms formed via Reaction (R3), likely due to the limited availability of Ti at the C/SiC–Ticusil interface as a result of Ti diffusion.

$$Ti + Cu \rightarrow TiCu \quad \Delta G = -60.9\ kJ/mol \qquad (R1)$$

$$Ti + 2Cu \rightarrow TiCu_2 \quad \Delta G = -58.9\ kJ/mol \qquad (R2)$$

$$5Ti + 3SiC \rightarrow Ti_5Si_3 + 3C \quad \Delta G = -587.1\ kJ/mol \qquad (R3)$$

$$Ti + C \rightarrow TiC \quad \Delta G = -109.3\ kJ/mol \qquad (R4)$$

Gibbs free energy (ΔG) diagram for Reactions (R1)–(R4) is presented as Figure S3 for a temperature range of 700–1100°C. The negative ΔG values for R1 (−60.9 kJ/mol) and R2 (−58.9 kJ/mol) indicate that the formation of TiCu and $TiCu_2$ is thermodynamically feasible. On the C/SiC side, the highly negative ΔG values for R3 (−587.1 kJ/mol) and R4 (−109.3 kJ/mol) confirm the spontaneous formation of Ti_5Si_3 and TiC, respectively. These thermodynamic predictions are consistent with the phase formation observed in both the EDS and XRD analyses. Previous studies showed the formation of Nb_2C, TiC, and Ti_5Si_3 when brazing C/SiC

to C103 using Ticusil filler.[6] However, this study observed the formation of TiCu and $TiCu_2$ instead of Nb_2C. This difference can be attributed to a significant increase in interphase thickness, which is four times greater in the current study. The increased interphase thickness effectively limited Nb diffusion from the C103 alloy to the C/SiC composite, as shown in Figure 2C, where Nb remains largely confined to the C103 substrate. Conversely, the C103–filler interface experienced Ti enrichment, resulting in the formation of IMCs, that is, TiCu and $TiCu_2$.[28] Additionally, the limited availability of Ti at the C/SiC interface leads to the precipitation of excess carbon. A thinner interphase facilitates easier diffusion and minimizes the formation of IMCs. Conversely, an excessively thick interphase can restrict Nb diffusion and promote Ti enrichment. The mismatch in CTE between the Ti-containing products and the C/SiC composite, combined with the presence of free carbon near the C/SiC interface, results in concentrated thermal residual stresses that contribute to crack formation.

Joint J-W1D1S1, with GLS dimensions of 1 mm for width, depth, and spacing, has a GSI of 1.8. The cross-sectional optical image of J-W1D1S1, as shown in Figure 3A, reveals that the grooves are effectively filled with filler alloy, forming metallic dentation. No voids, cracks, or defects are observed, which indicates sufficient flowability and the appropriate viscosity of the molten filler at the brazing temperature. This characteristic is crucial for brazing applications involving C/SiC, as inadequate flowability could leave the grooves unfilled, while excessive flowability could cause the molten braze to spill out, leaving parts of the GLS unsealed. Both scenarios could result in uneven distribution of residual stresses, deteriorating the mechanical properties of the joint.[23] Residual stress simulations, discussed in detail later, focused on specific regions of interest highlighted by three white rectangles in Figure 3A: the straight portion (SP) in rectangle b, the corner of the groove start (CGS, rectangle d), and the corner of the groove end (CGE, rectangle c). These areas are of particular importance due to the notable microstructural changes that occur, especially in terms of metal–metal interactions and metal–ceramic bonding at the corners of the groove. SEM-EDS analysis of these critical locations (SP, CGS, and CGE) for J-W1D1S1 shows that the interphase between the C103 alloy and the C/SiC composite, measuring ~165 μm thick, displays excellent bonding. The EDS point analysis, summarized in Table S2, confirms that the phase composition in the SP region of J-W1D1S1 is similar to that of a flat joint. At the CGE, the SEM-EDS images (Figure 3C) highlight infiltration of the filler into the micropores of the C/SiC, where Ti, Si, C, and a small amount of Ag are detected. This suggests the formation of thermodynamically stable high-temperature ceramics (HTCs) like TiC and Ti_5Si_3, which enhance the mechanical strength of the joint and reduce thermal residual stresses. Additionally, the formation of tiny nail-like structures consisting of TiC and Ti_5Si_3 further strengthens the joint and helps alleviate thermal residual stresses.[29] At the CGS, the SEM-EDS images (Figure 3D) reveal a high concentration of Ti, Nb, Cu, and Ag, with the formation of brittle IMCs such as TiCu and $TiCu_2$. These IMCs are found to be more susceptible to crack generation due to their high CTE relative to the C/SiC composite. However, the brittle IMCs at the CGS remain a potential site for crack formation due to the mismatch in CTE values. Overall, the joint morphology shows excellent reinforcement at the metal–ceramic interface, especially in critical areas like the SP, CGS, and CGE, ensuring superior performance during LSS testing.

For the fabrication of J-W1D1S2, the groove spacing (s) was increased to 2 mm while keeping all other parameters identical to J-W1D1S1, leading to a lower GSI value of 1.6. Optical and SEM images of the J-W1D1S2 joint cross-section are displayed in Figure S4. The optical image (Figure S4A) shows strong bonding between the C103 alloy and the C/SiC composite, further corroborated by the SEM image in Figure S4B. Since the EDS results for all GLS-based joints, including J-W1D1S2, were found to be consistent with those of J-W1D1S1, they are omitted here for brevity. At the SP, the interphase thickness measures ~110 μm, accompanied by the formation of nail-like structures. Extensive pore infiltration is observed at the CGE in Figure S4C, indicating excellent bonding. However, cracks are visible at the CGS on the SiC side, as highlighted in Figure S4D. These cracks are formed likely due to the presence of IMCs, as seen in J-W1D1S1 (refer to Figure 3D-Ti), which generate high residual stresses due to their high CTE. The location and orientation of these cracks, as shown in the micrograph, suggest that they initiate at the filler–ceramic junction and propagate along the exterior SiC ceramic layer (parallel to the joint interface), rather than following the fiber direction (indicated by blue arrows in Figure S4D). The brittle nature of the SiC ceramics matrix makes them less effective in constraining crack propagation, likely caused by residual stresses from the CTE mismatch. In contrast, the SiC-coated fibers exhibit greater resistance to crack propagation due to their higher toughness.[30] Consequently, the cracks predominantly extend within the brittle SiC ceramic layer rather than through the fiber reinforcement, as illustrated in Figure S4D. The 1 mm groove spacing of J-W1D1S1 allows the filler alloy to penetrate more uniformly into the pores, promoting the formation of reinforcing phases. In contrast, the 2 mm groove spacing of J-W1D1S2 ensures good filling; however, it results in higher residual stress concentration at the CGS due to the formation of IMCs. This suggests that

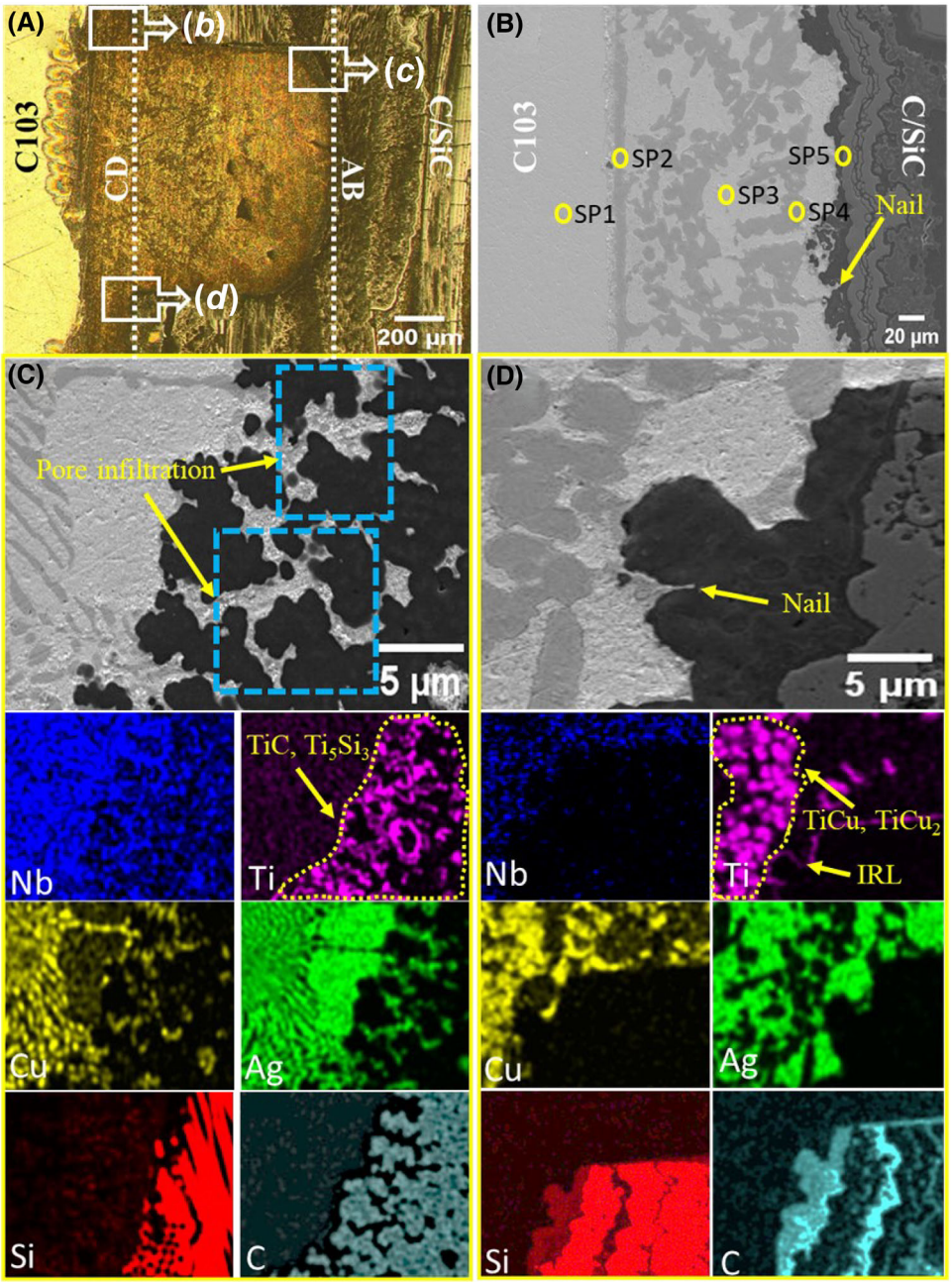

FIGURE 3 (A) Optical and (B–D) scanning electron microscopy with energy-dispersive X-ray spectroscopy (SEM-EDS) images of J-W1D1S1.

variations in groove spacing influence the microstructure, thereby affecting residual stress distribution and shear strength to different extents. Overall, the bond quality of J-W1D1S2 is good, but the presence of cracks at the CGS suggests its performance may be somewhat inferior to that of J-W1D1S1.

For J-W1D2S1, the groove depth (d) was increased to 2 mm, while for J-W1D2S2, both the depth (d) and spacing (s) were increased to 2 mm. Consequently, the GSI values for J-W1D2S1 and J-W1D2S2 are 2.3 and 1.8, respectively. The optical images and SEM micrographs for these joints are shown in Figure S5 (J-W1D2S1) and Figure S6 (J-W1D2S2). The interphase thicknesses were approximately 120 μm for J-W1D2S1 and 125 μm for J-W1D2S2, displaying morphologies similar to those of J-W1D1S2. The pore infiltration and formation of nail-like structures contributed to enhancing the bond strength in both configurations. However, the presence of cracks, particularly at the CGS, raises concerns about the overall bond integrity. These cracks, observed in previous joint configurations, suggest that residual stresses at the CGS may continue to affect the long-term performance of the joints. Increasing the groove depth from 1

mm to 2 mm enhanced braze filling, resulting in longer dentation and improved reinforcement for J-W1D2S1 and J-W1D2S2. However, the joints experienced shear strain-induced bending of the dentation, leading to premature failure and lower shear strength values.

The J-mixed configuration incorporates features from both J-W1D1S1 and J-W1D1S2 while retaining the original lap area of 10 mm × 10 mm. The resulting GSI value is 1.6, which is lower than J-W1D1S1 but identical to J-W1D1S2. Optical microscopy and SEM images of the J-mixed joint are shown in Figure S7. The optical image highlights strong bonding with noticeable pore infiltration. SEM analysis reveals an interphase thickness of around 155 μm. A closer look at the SP region (Figure S7B) at higher magnification shows a continuous crack along the SiC ceramic matrix near the filler–C/SiC interface. This crack formation, which was not present in previously discussed GLS-based joints, indicates that high residual stresses generated during the brazing process likely caused the cracks at the filler–C/SiC interface. Other characteristics, such as pore infiltration (Figure S7C) and crack formation at CGS, are consistent with those seen in GLS-based joints. Among all the joints, J-W1D1S1 shows the highest joint quality, with no cracks or defects. In contrast, J-mixed exhibits the poorest bond quality among the GLS joints, with cracks present at multiple interface locations (SP and CGS).

3.2 | Simulation of residual stresses

Numerical simulations were conducted to analyze the residual stresses during the brazing process, encompassing heating, cooling, and the application of confining pressure. The primary aim was to evaluate the geometric influence of specifically their width, depth, and spacing on joint performance. Comparative analyses were also performed with flat-type joints to highlight differences in residual stress distribution and overall joint behavior. To gain a deeper understanding of the strengthening mechanism in GLS-based joints, the normal and shear stresses along paths AB and CD, which are parallel to the filler dentation and represent the symmetry axes of the joining interface (as shown in Figure 1C,D), were analyzed concerning the geometric parameters of the GLS.

3.2.1 | Effect of GLS

The normal and shear stress distributions along path AB for the J-flat joint are shown in Figure 4. Elevated stress concentrations at the joint corners are attributed to the significant thermal expansion mismatch between the filler and the C103 alloy, leading to high normal and shear

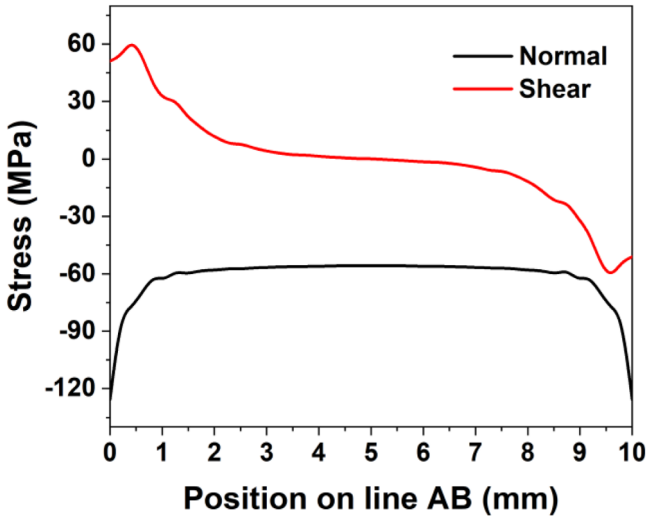

FIGURE 4 Stress distribution along path AB for J-flat.

stresses. In contrast, minimal or no shear stresses are observed along the central joining surface. At the beginning of the corner (0 mm on the AB line), the normal stress reaches a highly compressive value of −120 MPa, which rapidly decreases to −60 MPa at 1.5 mm from the corner and remains stable until 8.5 mm, after which it returns to −120 MPa. The shear stress exhibits opposing signs at both ends of the joint, peaking at −60 MPa. Despite increased stress levels, the opposing shear forces are neutralized in global behavior and do not contribute to failure. However, in the middle of the interface, where shear stress is near zero and normal stress is tensile in nature, microcracks begin to initiate along the filler–C/SiC interface, as confirmed by SEM analysis (inset of Figure 2B). EDS analysis further indicates that this region is particularly susceptible to stress concentration due to the presence of IMCs and free carbon, which makes it a critical site for crack initiation. The contour plots for equivalent stress in the flat joint, depicted in Figure 7A (discussed later), demonstrate a significant concentration of stresses along the interface.

The equivalent stress distribution along the *y*-direction of the joint is shown in Figure S8 for both J-flat and J-W1D1S1 configurations. At the joint center, the equivalent stress for the J-flat joint was approximately 420 MPa, increasing gradually to about 525 MPa at the edge (5 mm). However, the inclusion of GLS reversed this trend. For the J-W1D1S1 joint, the stress at the center slightly increased to around 450 MPa but dropped significantly to approximately 325 MPa at the edge. These results demonstrate the effectiveness of GLS in substantially reducing equivalent stress, particularly at the joint edges, which are common sites for debonding. In Figure 5, the stress distribution along paths AB and CD for the J-W1D1S1 joint is illustrated, with vertical gray strips representing the positions of the

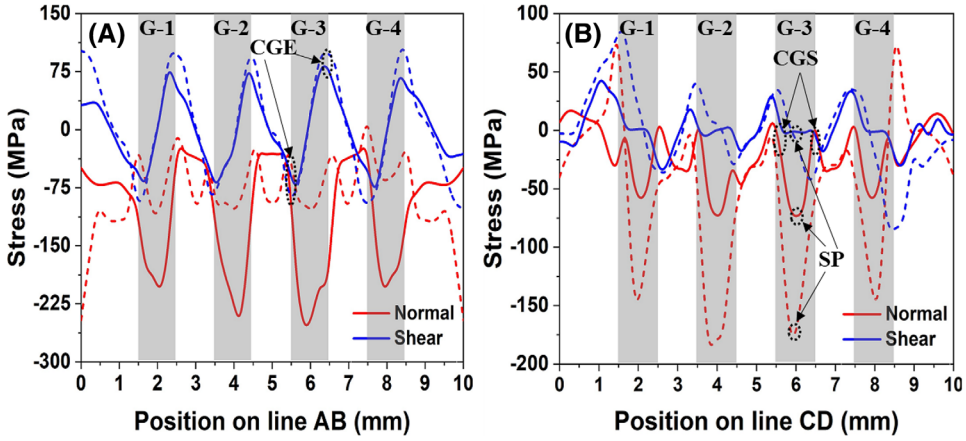

FIGURE 5 Stress distribution along the path (A) AB and (B) CD for J-W1D1S1 and J-W1D2S1 configuration.

grooves and the locations of SP, CGS, and CGE marked. Unlike the J-flat joint, the J-W1D1S1 joint exhibits oscillating normal stress due to its GLS configuration. Along the AB line, the normal stress varies significantly, ranging from −275 MPa to −40 MPa. The higher compressive stress at the SP interface (−275 MPa), compared to J-flat (−120 MPa), effectively impedes crack propagation, as evidenced by the absence of cracks in the SEM images (Figure 3). The compressive stress within the side grooves (G1 and G4) is around −200 MPa, while the middle grooves (G2 and G3) experience more compressive stress, between −250 MPa and −270 MPa. The shear stress along the AB line fluctuates between ±60 MPa, reversing direction at the ends of the grooves. Despite the presence of IMCs at CGS, the combination of higher compressive normal stress and opposing shear stress at the groove ends prevents crack propagation.

Along the CD line, the normal stress ranges from −60 to +10 MPa, and the shear stress from −50 to +40 MPa. Similar to the AB line, the center of the GLS along path CD experiences highly compressive normal stress, while the ends are subject to slight tensile stress. However, the stress magnitudes along CD are significantly lower than those along AB. Despite the presence of opposing shear stresses at both ends, crack propagation is unlikely, as this region lies within the dentated area of C103, as confirmed by the absence of cracks in the SEM images at CGE (Figure 3). The contour patterns of equivalent stress (Figure 7B) confirm that not only has the stress concentration at the interface decreased, but it has also resulted in the formation of stress bulbs both above and below the grooves. Thus, the results indicate that the incorporation of a GLS design offers significant advantages over flat joints, including improved anchoring, reduced residual stresses, and the formation of a shear stress couple. These factors are expected to enhance joint integrity and overall mechanical performance.

3.2.2 | Effect of GLS spacing

Joint J-W1D1S2, featuring a wider 2 mm groove spacing and a lower GSI of 1.6, has fewer grooves and a smaller lap area compared to J-W1D1S1. As illustrated in Figure 6A, the normal stress along path AB remains compressive throughout, oscillating between −275 MPa and −10 MPa, closely resembling the stress behavior observed in J-W1D1S1. Along path CD, the normal stress begins with a low tensile value (~10 MPa) in the first millimeter, then transitions to a compressive state (−70 MPa) for the majority portion of the joint. At the edge of the third groove (G-3), the stress reverses to a highly tensile state, peaking at 70 MPa. The shear stress along line AB varies from −50 MPa to +90 MPa, exceeding the intensities observed in J-W1D1S1, while still following an oscillating pattern between the grooves. This increased shear stress raises the likelihood of transverse deformation in the dentation, heightening the risk of de-bonding at the metal–ceramic interface. However, SEM images at CGE confirm the absence of crack initiation along path AB, despite the elevated normal and shear stresses. The resistance to cracking of the joint is attributed to the opposing shear stresses that effectively lock the joint and the extensive pore infiltration of molten braze forming HTCs, which alleviate stress, as supported by recent studies.[31,32] Cracks tend to form near the CGS in the C/SiC interface due to the presence of brittle IMCs. These IMCs lead to a mismatch in the CTE, causing differential volume changes during cooling. The larger groove spacing in J-W1D1S2 reduces the contact area at the joint interface, thereby amplifying shear stresses and increasing susceptibility to crack formation, particularly at the CGS. The equivalent stress concentration, as seen in Figure 7C, is particularly prominent along the interface between the grooves, suggesting that these areas are potentially vulnerable to fracture.

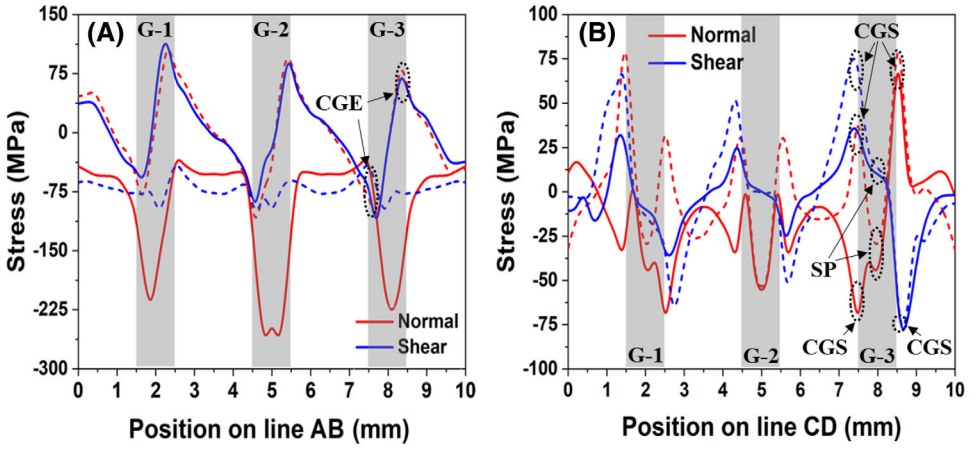

FIGURE 6 Stress distribution during the thermal process along path AB and CD for (A) J-W1D1S2 and (B) J-W1D2S2 configurations.

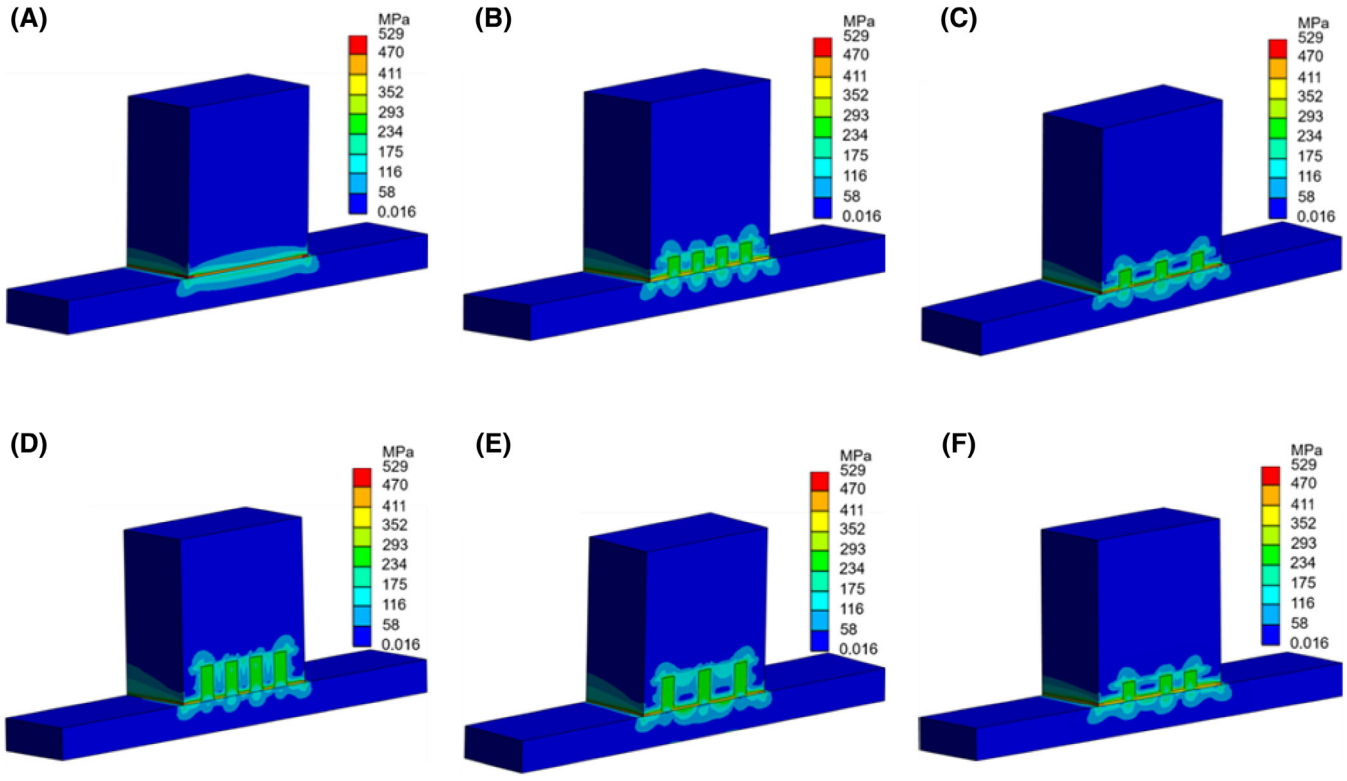

FIGURE 7 Equivalent stress contour for (A) J-flat, (B) J-W1D1S1, (C) J-W1D1S2, (D) J-W1D2S1, (E) J-W1D2S2, and (F) J-mixed.

3.2.3 | Effect of GLS depth

Joints J-W1D2S1 and J-W1D2S2 were fabricated with a groove depth of 2 mm, deeper than the 1 mm grooves in J-W1D1S1 and J-W1D1S2. This change increased the GSI to 2.3 for J-W1D2S1, while J-W1D2S2 maintained a GSI of 1.8, similar to J-W1D1S1. The normal and shear stress distributions along paths AB and CD for J-W1D2S1 and J-W1D2S2 are represented by dotted lines in Figures 5 and 6, respectively. For J-W1D2S1, the normal stress along path AB shows a significant reduction while remaining compressive, preventing crack initiation at the CGE. This behavior is confirmed by the SEM images in Figure S5C, which do not show crack formation at CGE. Along path CD, the normal stress becomes more compressive, ranging from −10 to −180 MPa, compared to J-W1D1S1. This increased compressive stress offers greater resistance to crack formation. However, the shear and normal stresses at the CGS are nearly negligible, leading to the formation of microcracks, as illustrated in Figure S5D. Furthermore, the

increased slenderness of the dentation, as shown in Figure S9 makes local buckling failure at the CGS a possibility. For J-W1D2S2, the normal stresses remain highly compressive, similar to J-W1D1S1, indicating a reduced likelihood of crack formation along path AB. As shown in Figure 5 for J-W1D2S1 and Figure 6 for J-W1D2S2, shear stress increased slightly along line AB but more substantially along line CD. Despite these changes, the oscillating shear stress pattern across the grooves persisted, as seen in previous joints. The increased shear stress, in both joints, leads to local buckling failure at both ends of the grooves, as illustrated in Figure S9. This increased groove stiffness, coupled with shear strain-induced bending of the dentation, could result in premature failure of the joint. Multiple cracks were observed at the CGS interface in the SEM images shown in Figures S5D and S6D, further supporting the presence of structural weaknesses due to stress concentration, enhanced shear forces, and local buckling failure near the ceramic–metal interface (path CD). Thus, J-W1D2S1 and J-W1D2S2 are likely to have reduced strength compared to J-W1D1S1, as these slender grooves lead to higher stress concentrations and deformation-induced failures. This is confirmed by the observation that the equivalent stresses are significantly concentrated around the CGS of each groove. This localized stress concentration underscores the influence of groove geometry on the stress distribution and overall joint performance.

3.2.4 | Effect of the mixed configuration

The J-mixed joint integrates design elements from J-W1D1S1 and J-W1D1S2, featuring a groove spacing of 1 mm on one half and 2 mm on the other. As shown in Figure S10, this hybrid configuration results in an uneven, nonsymmetric stress distribution along paths AB and CD compared to the more uniform stress profiles observed in J-W1D1S1. Despite this, the groove ceramic–metal interface at the CGE along path AB (Figure S7C) remains defect-free, largely due to the extensive pore infiltration of the molten braze and the formation of HTCs, which mitigate stress concentration. However, the stress unevenness is more pronounced at the groove corners and ceramic–metal interface along path CD, especially in the SP and CGS zones, where the presence of IMCs creates differential thermal expansion and contraction during cooling. This leads to stress localization and crack formation, as confirmed by the SEM images in Figure S7B. The combination of uneven stress distribution and IMC-induced stresses makes these zones, particularly SP and CGS, critical points for crack initiation. While the J-mixed joint performs better in terms of shear strength compared to J-flat, it underperforms relative to J-W1D1S1 and J-W1D1S2. The nonuniform

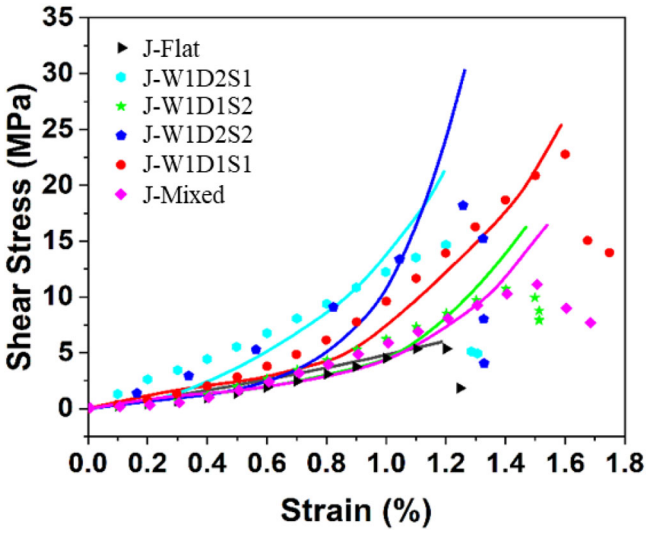

FIGURE 8 Load deformation curve for lap shear test with residual stresses.

groove configuration creates an asymmetric stress distribution, which weakens the bond strength of the joint, especially along path CD, where cracks develop at both SP and CGS. In line with this observation, the equivalent stress contours for the mixed configuration reveal notable asymmetry and elevated stress levels concentrated along the interface. This stress distribution highlights the impact of the mixed configuration on the mechanical behavior and potential stress localization within the joint. This unevenness compromises the overall integrity of the joint, making it less effective than uniformly spaced groove configurations in sustaining mechanical loads.

3.3 | Simulation of LSS test

The load–strain (LSS) behavior of six different joint configurations has been evaluated, both with and without considering residual stresses, as illustrated in Figures 8 and S11, respectively. Including residual stresses in the simulations results in better alignment with experimental data, especially by capturing the nonlinear load-deformation behavior. This improvement is attributed to the incorporation of geometric irregularities arising from the heating and cooling cycles during the brazing process, which were effectively captured in the simulation by including residual stresses. A comparison of the LSS curves from simulations with and without thermal analysis, shown in Figures 8 and S11, respectively, highlights a significant disparity, with simulations excluding residual stresses showing poor agreement with experimental data. Consequently, as the LSS simulation results without residual stresses fail to accurately represent the behavior of the system, they are

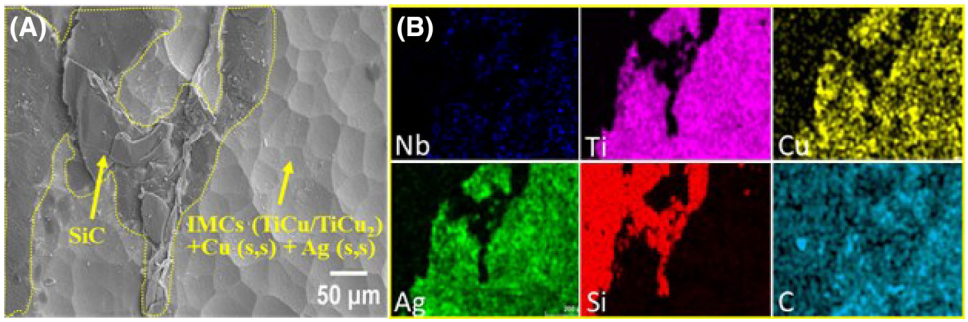

FIGURE 9 (A) Scanning electron microscopy (SEM) image and (B) energy-dispersive X-ray spectroscopy (EDS) mapping of the fracture surface of J-flat.

excluded from further analysis. For most joints, the deviation between simulation and experimental results is less than 10%. However, for joints J-W1D2S1 and J-W1D2S2, the deviation is slightly higher, approximately 15%, which may be attributed to the model's inability to fully capture the nonlinear hyperelastic behavior of the filler material.

The LSS curve for the flat joint reveals a relatively low strength of 6 ± 1.8 MPa and a corresponding strain of 1.2%. The poor performance of J-flat can be attributed to the significant difference in the CTE among the IMCs, C/SiC composite, and C103 alloy. This large mismatch in CTE during the cooling phase generates high residual stresses at the joint, which promote crack formation, as observed in Figure 2B. Due to the brittle nature of the IMCs present at the reaction zone (Figure 2C), these cracks propagate rapidly when the joint is subjected to loading, leading to premature failure. The fracture surface analysis from the LSS test further corroborates this failure mechanism. The microstructure and chemical composition of the fracture surface of the flat joint, as shown in Figure 9 confirm that the joint failure occurred at the interface between the C/SiC composite and the IMCs. EDS mapping (Figure 9B) highlights the presence of SiC fragments attached to the fracture surface, indicating that the crack propagation originated at the C/SiC-IMC interface. The dotted yellow line in Figure 9A further delineates the fracture path. These observations confirm the hypothesis that pre-existing cracks, which formed during the brazing process, severely compromised the strength of the J-flat joint. The lower elastic strain energy values observed in the stress path simulation (Figure 10) suggest a potential for crack initiation along the joint surface. This, coupled with the concentrated equivalent stress (Figure 7) at the joint surface in the thermal analysis and the minimal change in strain energy (<10%) in the LSS simulation, further supports the occurrence of cracking during the brazing process.

Introducing grooves into the joint interface, as illustrated in J-W1D1S2, improves performance. The LSS of J-W1D1S2 rises to 11.3 MPa, along with increased stiffness. This enhancement is due to several factors, including an increased GSI (1.6 compared to 1 for J-flat), a larger lap area, reduced residual stress during cooling, the balancing of tensile and compressive stresses, and the mechanical anchoring effect of the grooves. Joints with larger interfacial contact areas, such as J-W1D2S2 (14.7 MPa) and J-W1D2S1 (18.8 MPa), show superior bonding performance. Despite having deeper grooves, J-W1D2S2 exhibits lower stiffness and strength compared to J-W1D2S1. The high energy release rates observed in the stress paths of both J-W1D2S2 and J-W1D2S1 further support the initiation and propagation of cracks during the LSS test, indicating brittle failure. SEM images at CGS revealed similar crack propagation patterns at the IMCs and C/SiC interfaces across all joints.

J-W1D1S1 achieves the highest LSS of 22.8 ± 1.5 MPa among all configurations, attributed to its uniformly distributed residual stress within the joint, as illustrated in Figures 5 and 7. The even distribution of stress, combined with the favorable interaction between nonzero shear stress and high compressive stress, contributes to its superior shear performance, as confirmed by SEM analysis (Figure 3), even in CGS. SEM-EDS analysis was utilized to examine the failure mechanisms of LSS specimens by analyzing their fracture surfaces, with results shown in Figure 11. A substantial portion of the fracture surface is occupied by the SiC matrix and carbon fibers, as indicated in Figure 11A. The feature marked by a black dotted circle in Figure 11A was identified as a (Cu, Ag, Nb) ss "pore infiltration" through EDS analysis (see Figure 11C). Surrounding this pore infiltration, an IRL primarily composed of TiC and Ti_5Si_3 (HTCs) formed due to the reaction of Ti with the C/SiC matrix. A closer look at Figure 11A revealed debonding at the ceramic–metal interface during the LSS test. Notably, the opposite side of the pore infiltration remained intact, indicating a strong bond in J-W1D1S1. The composite fractured under load, with cracks initiating near the composite material (Figure 11A), leading to

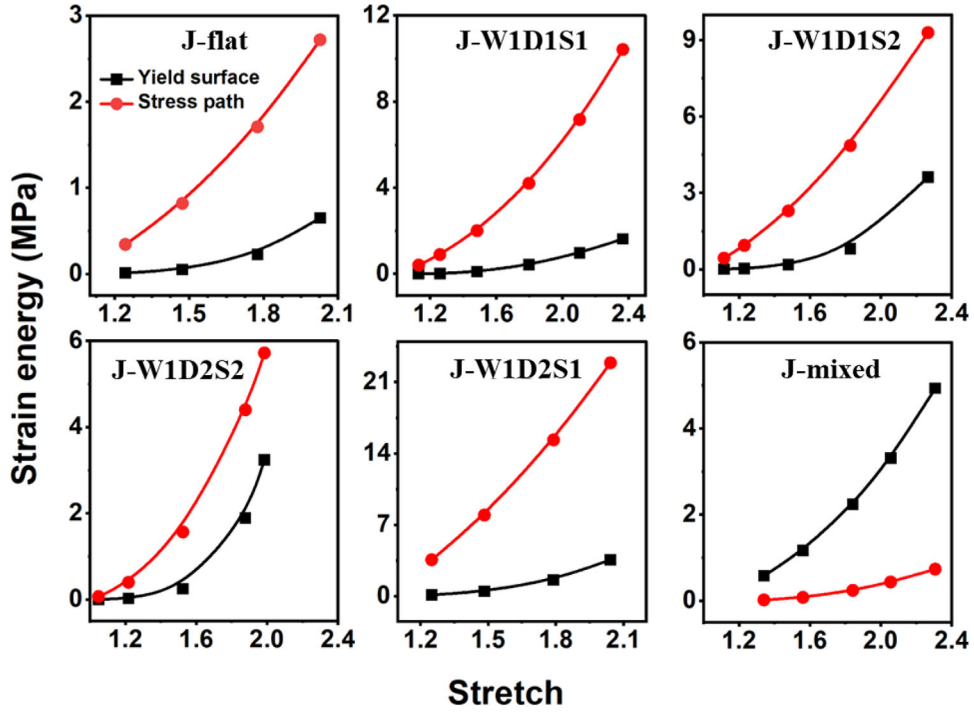

FIGURE 10 Stress path predicted by lap shear strength (LSS) simulation (with residual stresses) for all joint configurations.

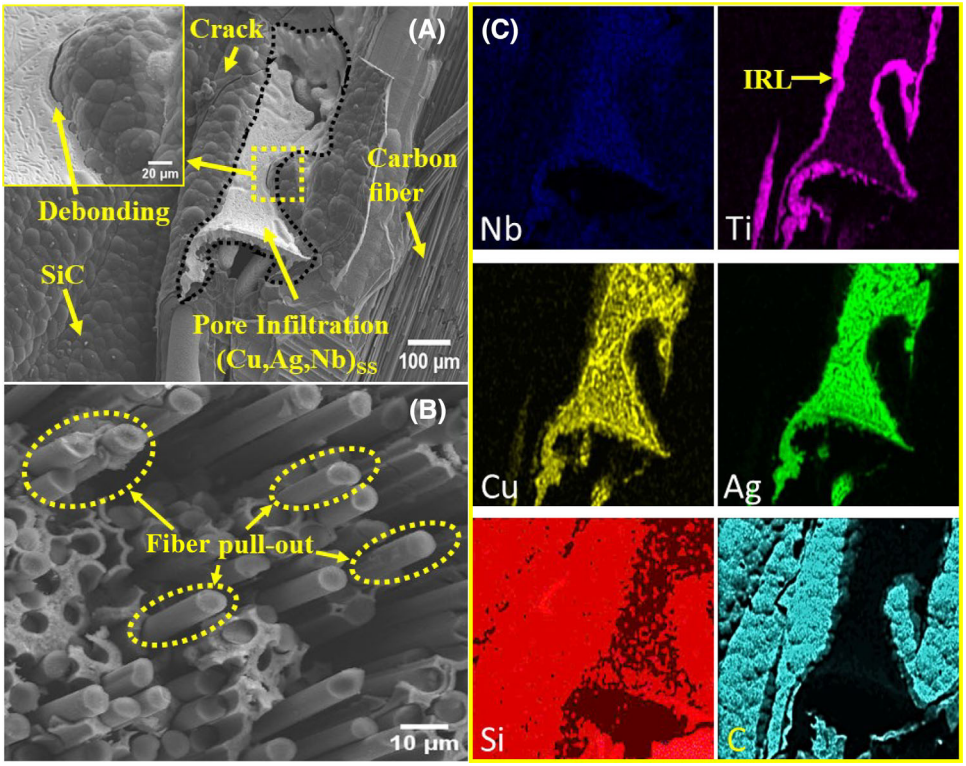

FIGURE 11 (A, B) Scanning electron microscopy (SEM) images and (C) energy-dispersive X-ray spectroscopy (EDS) mapping of the fracture surface of J-W1D1S1.

TABLE 3 Phases, residual stresses, crack possibilities, and strength for all joints.

Joint	Primary phases (experimental)			Residual stresses (simulation)			Crack possibility (simulation)			Crack presence (experimental)			LSS (MPa)
	SP	CGS	CGE	SP	CGS	CGE	SP	CGS	CGE	SP	CGS	CGE	
J-flat	HTC + IMC	-	-	LC	-	-	H	-	-	Yes	-	-	LL (6.0)
J-W1D1S1	HTC	IMC	HTC	C	LC	HC	L	L	L	No	No	No	HH (22.8)
J-W1D1S2	HTC	IMC	HTC	C	LC	C	L	H (M1)	L	No	Yes	No	L (11.3)
J-W1D2S1	HTC	IMC	HTC	HC	T	C	L	H (MM)	L	No	Yes	No	HH (18.8)
J-W1D2S2	HTC	IMC	HTC	LC	T	C+T	L	H (M1)	H (MM)	No	Yes	No	H (14.7)
J-mixed	HTC	IMC	HTC	LC	C+T	HC	L	H/L[a] (M1)	H (MM)	Yes	Yes	No	L (11.2)

Abbreviations: C, compressive; CGE, corner of the groove end; CGS, corner of the groove start; H, high; HC, highly compressive; HH, very high; HTC, high-temperature ceramic phases; IMC, intermetallic compound; L, low; LC, low compressive; LL, very low; LSS, lap shear strength; SP, straight portion; T, tensile.
[a]Depending on the groove spacing. The bracketed entries M1 and MM represent mode one and mixed mode failure.

extensive fiber pull-out (Figure 11B). The energy absorbed during the process raised the fracture limit of J-W1D1S1 to 22.8 MPa, which is nearly 99% of the strength of the C/SiC substrate. The failure predominantly manifested the toughening of joints due to GLS resulting in a great leap in the bond strength. J-W1D1S1 exhibits the lowest energy release rate and change in strain energy (see Figure 10), suggesting elastic material behavior and a slower approach to failure. The gentler slope of the stress path in J-W1D1S1 in Figure 10 further supports a ductile failure mechanism. Additionally, the deviation from the yield surface indicates that the specimen has not yet experienced cracking along the joint surface.

During cooling, the J-mixed joint undergoes imbalanced tensile and compressive forces at the interface, as illustrated in Figure S10. With an LSS of 11.2 MPa, it represents the weakest point among GLS-based joints, primarily due to crack formation at the SP and CGS. While increasing the groove spacing in GLS-based joints enhances their stiffness, it also raises the likelihood of brittle failure, which is confirmed in a stress path with a higher slope value of stress path in Figure 10. Unlike the compression-induced failures observed in J-W1D1S1 and J-W1D1S2, J-W1D2S1 and J-W1D2S2 experienced bending failures due to the greater groove depth. Although deeper grooves increase stiffness, they reduce the overall strength of the joint due to the dominance of local buckling in the failure mechanism.

Table 3 summarizes the stresses, compositions, crack probabilities, and experimental observations at critical points of the joints. Insufficient mechanical anchoring in J-flat, coupled with an extensive IMC reaction zone and tensile residual stress results in process-induced microcracks prone to nucleate and expand under LSS testing, resulting in a low value of 6 MPa. For GLS-based joints (J-W1D1S2, J-W1D2S1, and J-W1D2S2), a compressive normal stress generated due to the dentation structure, transforms the SP region into a crack-free zone. This SP region, along with the CGE, witnessed the formation of HTCs. However, the CGS remains a concern due to the formation of IMCs, which have much higher CTE compared to the C/SiC, causing microcrack generation during cooling. These cracks at CGS may trigger joint debonding due to local buckling-dominated failure under eccentric loading. Nonetheless, GLS-based joints outperformed J-flat due to the periodic fluctuation of residual stress resulting from to dentation structure. The J-mixed configuration experienced asymmetric stresses along the joining interface, leading to a high probability of crack formation at the locations with a concentration of equivalent stress in Figure 7 (J-mixed). Consequently, cracks developed at multiple locations, including SP and CGS, which propagated during testing, resulting in the lowest LSS of 11.2 MPa among GLS-based joints. In contrast, J-W1D1S1 proved to be an exceptional joint, characterized by HTC formation at SP and CGE, and IMCs at CGS. Thanks to uniformly distributed compressive stresses, no cracks developed at CGS despite the presence of IMCs, which lowered the crack generation probability. As a result, J-W1D1S1 exhibited the highest LSS of 22.8 MPa, with failure occurring in the C/SiC substrate while the metal–ceramic bond remained intact. The LSS of the joints follows the trend: J-W1D1S1 > J-W1D2S1 > J-W1D2S2 > J-W1D1S2 > J-mixed > J-flat.

4 | CONCLUSIONS

The introduction of GLS onto the joining surface of C/SiC composites and C103 alloy, using Ticusil active braze alloy, was shown to significantly enhance the mechanical performance of ceramic–metal brazed joints compared to traditional flat joints. This improvement was primarily due to the redistribution of stress concentrations,

with the majority of stress transferred to the C103 alloy. The significance of groove width, depth, and spacing in joint microstructure, residual stress distribution, and LSS behavior was highlighted through experimental analysis combined with FEA validation. In the dentation regions of the C103 alloy formed by the GLS geometry, the critical points for crack initiation were determined and examined concerning varying GLS configurations. The stress path was created from simulations of the LSS tests, depicting the progression of stress in all GLS configurations. It has been found that the formation of brittle IMCs (TiCu and $TiCu_2$) near the brazing seam, due to the abundance of reactive elements, contrasted with the HTC phases (TiC and Ti_5Si_3) formed at the metal–ceramic interface, further illustrating the complex interplay of phases affecting joint reliability. The optimal GLS configuration, featuring a 1 mm groove depth, width, and spacing was identified which successfully minimized residual shear stresses while increasing compressive normal stresses, reversing shear stress direction, and enlarging the joining area. This synergy between mechanical anchoring and stress redistribution greatly enhanced the load-bearing capacity of the joint compared to flat joint configurations. The findings of this study have important implications for industries such as nuclear, automotive, defense, and optics, where the integrity and reliability of ceramic–metal brazed joints are crucial. The GLS method offers a promising avenue for improving joint strength, durability, and reliability, paving the way for advancements in ceramic–metal joining technology across these sectors.

ACKNOWLEDGMENTS

The authors thank Buragadda V. Rajasekhar (Section Head, CMTS), Renjith Devasia (Head, CMPD), Vinu Viswanath (GD, CMDG), and Sunil P. (DD, CMSE) for their encouragement and the Analytical and Spectroscopy Division of VSSC for their support in material characterization.

ORCID

Anurag Kamal https://orcid.org/0000-0002-7001-8543
Vijay M. Shinde https://orcid.org/0000-0001-9289-0271

REFERENCES

1. Naslain RR. SiC-matrix composites: nonbrittle ceramics for thermo-structural application. Int J Appl Ceram Technol. 2005;2(2):75–84. https://doi.org/10.1111/j.1744-7402.2005.02009.x
2. Buffenoir F, Zeppa C, Pichon T, Girard F. Development and flight qualification of the C–SiC thermal protection systems for the IXV. Acta Astronaut. 2016;124:85–89. https://doi.org/10.1016/j.actaastro.2016.02.010
3. Salvo M, Ferraris M, Lemoine P, Montorsi MA, Merola M. Joining of CMCs for thermonuclear fusion applications. J Nucl Mater. 1996;233:949–53. https://doi.org/10.1016/S0022-3115(96)00148-1
4. Heinrich JG, Aldinger F. Multilayer C/SiC composites for automotive brake systems. In: Gadow R, Speicher M, editors. Ceramic materials and components for engines. Wiley-VCH; Germany, 2001. p. 565–70. https://doi.org/10.1002/9783527612765.ch96
5. Harnisch B, Kunkel B, Deyerler M, Bauereisen S, Papenburg U. Ultra-lightweight C/SiC mirrors and structures. ESA Bull. 1998;95:5–8.
6. Kamal A, Shukla AK, Shinde VM, Rajasekhar BV. Microstructure and mechanical properties of C/SiC-niobium alloy (C103) joint brazed with TiCuAg alloy for aerospace applications. Ceram Int. 2023;49:29265–73. https://doi.org/10.1016/j.ceramint.2023.06.218
7. Asthana R, Singh M. Joining of ZrB_2-based ultra-high-temperature ceramic composites using Pd-based braze alloys. Scr Mater. 2009;61:257–60. https://doi.org/10.1016/j.scriptamat.2009.03.053
8. Tatarko P, Chlup Z, Mahajan A, Casalegno V, Saunders TG, Dlouhy I, et al. High-temperature properties of the monolithic CVD β-SiC materials joined with a pre-sintered MAX phase Ti_3SiC_2 interlayer via solid-state diffusion bonding. J Eur Ceram Soc. 2017;37(4):1205–16. https://doi.org/10.1016/j.jeurceramsoc.2016.11.006
9. Xiong J, Li J, Zhang F, Huang W. Joining of 3D C/SiC composites to niobium alloy. Scr Mater. 2006;55:151–54. https://doi.org/10.1016/j.scriptamat.2006.03.050
10. Tatarko P, Casalegno V, Hu C, Salvo M, Ferraris M, Reece MJ. Joining of CVD-SiC coated and uncoated fibre-reinforced ceramic matrix composites with pre-sintered Ti_3SiC_2 MAX phase using spark plasma sintering. J Eur Ceram Soc. 2016;36:3957–67. https://doi.org/10.1016/j.jeurceramsoc.2016.06.025
11. Kamal A, Shukla AK, Shinde VM, Yadav SD. Effect of Mo addition on interfacial microstructure and mechanical property of SiC joint brazed by an Ni–Si filler. J Am Ceram Soc. 2024;107:2861–76. https://doi.org/10.1111/jace.19677
12. Jiang X, Zhang G, Zhang Y, He P. High-temperature brazing of C/C using hastelloy C-276 as filler and joint formation mechanism. Compos-A. 2023;168:107487. https://doi.org/10.1016/j.compositesa.2023.107487
13. Ba J, Ji X, Wang B, Li P, Lin J, Qi J, et al. Root-like C/SiC surface structure fabricated by the thermal and electrochemical corrosion for brazing to Nb. Compos B Eng. 2021;218:108942. https://doi.org/10.1016/j.compositesb.2021.108942
14. Tian X, Feng J, Shi J, Liu Y, Zhang L. Interfacial microstructure and mechanical properties of the vacuum brazed C/SiC composite and Nb joints. Vacuum. 2017;146:97–105. https://doi.org/10.1016/j.vacuum.2017.09.039
15. Zhang K, Zhang L, He R, Wang K, Wei K, Zhang B. Joining of Cf/SiC ceramic matrix composites: a review. Adv Mater Sci Eng. 2018;2018:6176054. https://doi.org/10.1155/2018/6176054
16. Zhang Q, Sun L, Liu Q, Zhang J, Wang T, Liu C. Effect of brazing parameters on microstructure and mechanical properties of Cf/SiC and Nb-1Zr joints brazed with Ti-Co-Nb filler alloy. J Eur Ceram Soc. 2017;37:931–37. https://doi.org/10.1016/j.jeurceramsoc.2016.09.031
17. Wang Y, Wang W, Huang J, Zhou S, Yang J, Chen S. Composite brazing of C/C composite and Ni-based superalloy using (Ag-10Ti)+TiC filler material. J Mater Process

Technol. 2021;288:116886. https://doi.org/10.1016/j.jmatprotec.2020.116886
18. Cui B, Huang JH, Xiong JH, Zhang H. Reaction-composite brazing of carbon fiber reinforced SiC composite and TC4 alloy using Ag–Cu–Ti–(Ti+C) mixed powder. Mater Sci Eng A. 2013;562:203–10. https://doi.org/10.1016/j.msea.2012.11.031
19. Ba J, Zheng XH, Ning R, Lin JH, Qi JL, Cao J, et al. C/SiC composite-Ti_6Al_4V joints brazed with negative thermal expansion ZrP_2WO_{12} nanoparticle reinforced AgCu alloy. J Eur Ceram Soc. 2019;39:755–61. https://doi.org/10.1016/j.jeurceramsoc.2018.12.028
20. Kamal A, Shukla AK, Shinde VM. High-strength C/SiC joints prepared using a novel Ni-Si-CNTs-based filler. J Eur Ceram Soc. 2023;43:7411–21. https://doi.org/10.1016/j.jeurceramsoc.2023.08.024
21. Lin JH, Luo DL, Chen SL, Mao DS, Wang ZY, Ma Q, et al. Control interfacial microstructure and improve mechanical properties of TC_4-SiO_2f/SiO_2 joint by AgCuTi with Cu foam as interlayer. Ceram Int. 2016;42:16619–25. https://doi.org/10.1016/j.ceramint.2016.07.084
22. Hernandez X, Jimenez C, Mergia K, Yialouris P, Messoloras S, Liedtke V, et al. An innovative joint structure for brazing Cf/SiC composite to titanium alloy. J Mater Eng Perform. 2014;23:3069–76. https://doi.org/10.1007/s11665-014-1074-9
23. Xiong JT, Li JL, Zhang FS, Lin X, Huang WD. Direct joining of 2D carbon/carbon composites to Ti–6Al–4V alloy with a rectangular wave interface. Mater Sci Eng A. 2008;488:205–13. https://doi.org/10.1016/j.msea.2007.11.013
24. Yang ZW, Wang CL, Han Y, Zhao YT, Wang Y, Wang DP. Design of reinforced interfacial structure in brazed joints of C/C composites and Nb by pre-oxidation surface treatment combined with in situ growth of CNTs. Carbon. 2019;143:494–506. https://doi.org/10.1016/j.carbon.2018.11.047
25. Zhan CT, Wu JY, Huang KH, Li Y, Wu L-X, He S-J, et al. Joining of textured PLS-SiC ceramic with CaO-Al_2O_3-MgO-TiO_2-SiO_2 glass filler. Ceram Int. 2024;50:495–502. https://doi.org/10.1016/j.ceramint.2023.10.125
26. Lohr MJ, Sugerman GP, Kakaletsis S, Lejeune E, Rausch MK. An introduction to the Ogden model in biomechanics: benefits, implementation tools and limitations. Philos Trans R Soc A. 2022;380(2233):20210365. https://doi.org/10.1098/rsta.2021.0365
27. Kawecki A, Knych T, Sieja-smaga E, Mamala A, Kwaśniewski P, Kiesiewicz G, et al. Fabrication, properties and microstructures of high strength and high conductivity copper-silver wires. Arch Metall Mater. 2012;57:1261–70. https://doi.org/10.2478/v10172-012-0141-1
28. Lee MK, Lee JG, Lee JK, Park JJ, Lee GJ, Uhm YR, et al. Strong bonding of titanium to copper through the elimination of the brittle interfacial intermetallics. J Mater Res. 2008;23:2254–63. https://doi.org/10.1557/JMR.2008.0269
29. He Z, Sun L, Li C. Wetting and brazing of Cf/C composites with SieZr eutectic alloys: The formation of nano- and coarse-SiC reaction layers. Carbon. 2020;167:92–103. https://doi.org/10.1016/j.carbon.2020.05.109
30. Xu Y, Cheng L, Zhang L, Yin H, Yin X. Mechanical properties of 3D fiber reinforced C/SiC composites. Mater Sci Eng A. 2001;300:196–202. https://doi.org/10.1016/S0921-5093(00)01533-1
31. Guo X, Si X, Liu Y, Zhao W, Wang X, Li C, et al. A chromium carbide coating in situ formed on C/C composites by the novel reactive wetting strategy to enhance oxidation resistance. J Eur Ceram Soc. 2022;42:6435–44. https://doi.org/10.1016/j.jeurceramsoc.2022.07.016
32. Sun L, Fang J, Guo S, Wen Y, Liu C, Zhang J. Joining dense Si_3N_4 to porous Si_3N_4 using a novel glass-ceramic interlayer with precipitated β-$LiAlSi_2O_6$/Mg_2SiO_4. J Eur Ceram Soc. 2022;42:87–95. https://doi.org/10.1016/j.jeurceramsoc.2021.09.050

SUPPORTING INFORMATION

Additional supporting information can be found online in the Supporting Information section at the end of this article.

How to cite this article: Kamal A, Pal MK, Shinde VM, Jadhav AB, Shukla AK. Effect of groove-like structures on residual stress and shear strength in C/SiC–C103 alloy joints. J Am Ceram Soc. 2025;108:e20547. https://doi.org/10.1111/jace.20547